https://doi.org/10.5194/essd-2025-836
Preprint. Discussion started: 18 March 2026

Open Access Earth System Science Data Discussions

A database of objectively identified atmospheric rivers based on a multi-method fusion algorithm

Hongbin Chen[1], Jian Rao[1], Seok-Woo Son[2], Bin Guan[3], and Mengxin Pan[4]

[1]State Key Laboratory of Environment Characteristics and Effects for Near-space, Nanjing University of Information Science and Technology, Nanjing, China
[2]School of Earth and Environmental Sciences, Seoul National University, Seoul, Republic of Korea
[3]Joint Institute for Regional Earth System Science and Engineering, University of California, Los Angeles, Los Angeles, California, USA
[4]Department of Geography, Simon Fraser University 8888 University Drive Burnaby, BC, V5A 1S6 Canada

Correspondence to: Jian Rao (raojian@nuist.edu.cn)

Abstract. Atmospheric rivers (ARs) are long, narrow corridors in the atmosphere that transport immense amounts of water vapor poleward across the mid-latitudes. On one hand, ARs can act as one of the precipitation sources, end drought, accumulate snowpacks, and support ecosystems and the society. One the other hand, ARs also represent a type of hazard and are responsible for economic losses, such as by extreme precipitation and winds, rain on existing snowpacks, or causing debris flows and landslides. Given the importance of ARs, this paper proposes a multi-method fusion algorithm for more objectively identifying ARs on a global scale. The proposed algorithm, based on the vertically integrated water vapor transport (IVT), integrates advanced strategies from multiple existing algorithms and introduces a dual-axis test method to enhance the stability of AR identification. Using IVT data from ERA5, a global AR database is constructed at a horizontal resolution of 1° × 1° and a time interval of six hours from 1940 to 2024. Comparative evaluation against established AR databases reveals strong agreement in mid-latitude ocean basins where ARs are most active. The usefulness of the new AR database is also demonstrated by examining the role of ARs in two extreme events in the recent past: atypical AR activity during the East Asian Meiyu rainfalls in late June 2018, and rare AR activity during the Australian Black Summer in late January 2020. The results show that the new AR database helps to reduce the uncertainty in AR identification and to better understand extreme events and their variations in time and space.

1 Introduction

The concept of atmospheric river (AR) was first introduced by Zhu and Newell (1994) to describe a now formally defined transient and narrow corridor of intense water vapor transport in the lower troposphere, typically associated with low-level jet streams ahead of the cold front of an extratropical cyclone (Ralph et al., 2018). The synoptic and climatological characteristics of ARs have been extensively examined in recent decades. It is now well documented that approximately a dozen ARs exist globally at any given time, each exceeding 2000 km in length, with a width less than half of the length and the core of water vapor centered at below 650 hPa (Guan and Waliser, 2015; Ralph et al., 2017b). ARs predominantly occur in the mid-latitudes

https://doi.org/10.5194/essd-2025-836
Preprint. Discussion started: 18 March 2026

and continuously transport substantial amounts of moisture poleward, accounting for over 90% of the total meridional water vapor transport across these latitudes (Zhu and Newell, 1998), thereby playing a significant role in the global water cycle.

When an AR makes landfall, the abundant moisture it carries can undergo condensation and precipitation due to orographic lifting over windward slopes (Ralph and Dettinger, 2011). This process can lead to intense rainfall events, which have dual effects on the hydrology of different regions. On one hand, ARs can provide abundant water resources (Guan et al., 2010), helping to alleviate drought conditions (Dettinger, 2013). On the other hand, prolonged heavy precipitation associated with ARs may cause flooding, landslides, and other natural hazards (Neiman et al., 2011; Ralph et al., 2006). Due to the significant role of ARs in influencing precipitation and moisture distribution in the mid-latitudes, research on them has increased substantially in recent years (Ralph et al., 2017a), including but not limited to the relationship between ARs and extratropical cyclones (Guo et al., 2020; Zhang et al., 2019), AR-related precipitation and its impact (Chen et al., 2018; Kwon and Son, 2024; Paltan et al., 2017), as well as the projected response of ARs to climate changes (Corringham et al., 2022; Liang et al., 2023; Payne et al., 2020).

Early studies primarily focused on the AR activities along the west coasts of North America and Europe in the winter season (Lavers et al., 2011; Neiman et al., 2008). The typical AR phenomena are mostly accompanied by extratropical cyclones, which are located downstream of storm tracks. However, subsequent research has demonstrated that ARs can also appear when the extratropical cyclones are inactive (Gimeno et al., 2021). Furthermore, the water vapor transport core channels during the East Asian summer monsoon exhibit narrow and elongated structures, which can also be identified as ARs (Liang and Yong, 2021; Ye et al., 2020). It is suggested that the formation and maintenance of the East Asian summer ARs are influenced by multiple weather systems, including the southwest monsoon, extratropical cyclones, or a combination of both, with the western North Pacific subtropical high (WNPSH) playing a critical role in controlling the AR track and orientation (Park et al., 2021). Complex dynamics concerning the monsoon activities lead to multifaceted temporal variations in East Asian summer ARs, including low-frequency, high-frequency, and intermediate-frequency features (Park et al., 2023; Park and Son, 2024). The particularity of East Asian summer ARs illustrates that ARs remain to be better defined and theoretically understood.

As a technical foundation for AR research, current AR identification algorithms are primarily based on morphology of the water vapor transport corridors (Shields et al., 2018). These algorithms can be categorized from various perspectives: in terms of meteorological fields, they use either vertically integrated water vapor (IWV; Wick et al., 2013) or vertically integrated water vapor transport (IVT; Lavers et al., 2012) as the detection variable; regarding spatial scales, they encompass single-station (Ralph et al., 2013), regional (Nayak et al., 2014), and global scale (Guan and Waliser, 2015) methods; and from a tracking standpoint, they include Eulerian (instantaneous identification) algorithms (Brands et al., 2017), Lagrangian algorithms (Zhou et al., 2018), and comprehensive algorithms that combine both functions (Guan and Waliser, 2024; Pan and Lu, 2019). Notable discrepancies exist among AR algorithms in the selection of detection variables, threshold settings, and methods for characterizing AR features, potentially leading to inconsistent identifications of ARs. To quantify these differences and uncertainties and provide general guidance on algorithm choices for diverse research purposes, the Atmospheric River

https://doi.org/10.5194/essd-2025-836
Preprint. Discussion started: 18 March 2026

Tracking Method Intercomparison Project (ARTMIP) conducted systematic evaluations of a suite of AR identification algorithms (Rutz et al., 2019), offering critical insights for further developing and optimizing algorithms.

Numerous advanced AR identification algorithms have been constructed: the innovative designs in these algorithms reflect individual developers' understanding of ARs, and each has been demonstrated to have advantages in specific application scenarios. For global-scale AR identification at specified times from a Eulerian perspective, this study proposes a multi-method fusion algorithm that integrates advanced strategies from multiple existing algorithms (Brands et al., 2017; Guan et al., 2018; Guan and Waliser, 2024; Pan and Lu, 2019, 2020) and introduces a dual-axis test method in key steps to enhance identification stability. Based on this algorithm, an AR database is constructed and compared with selected existing AR databases to assess its performance, analyze inter-database differences, and discuss potential causes of these discrepancies. Furthermore, by examining the atypical AR activities during several recent extreme cases, the feasibility of this AR database generated by the proposed algorithm is verified.

2 Methods

In the scenario of identifying ARs at a specific time, existing algorithms are predominantly constructed upon an objective conditional identification framework. The steps of identifying ARs can be summarized as follows: for the detection variable capable of representing ARs, intensity thresholds are first applied to extract continuous regions with anomalously high values (hereafter, AR candidates) from the background field at the given time. Subsequently, these candidates are analyzed to quantify their key characteristics, particularly morphological attributes such as length, width, and curvature. Finally, the quantified metrics are evaluated against predefined criteria to identify those satisfying the conditions as ARs. This identification procedure aligns closely with the core requirements specified in the definition of AR for the intensity and morphological features of the water vapor transport corridor.

In terms of detection variable selection, both IWV and IVT have been employed for identifying ARs, and they are highly correlated in characterizing ARs (Neiman et al., 2008; Ralph et al., 2004). Nevertheless, studies have pointed out that IVT exhibits a greater inland penetration capability during the landfall process of ARs, thereby more effectively describing moisture transport associated with complex terrains (Neiman et al., 2002; Rutz et al., 2014). Furthermore, the vectorial property of IVT can well distinguish ARs from other high-moisture systems, such as tropical cyclones and zonally-oriented tropical moisture filaments. Tropical cyclones generally lack the typical filamentary structure and directional coherence in water vapor transport, while tropical moisture filaments typically do not exhibit appreciable poleward moisture flux, both differing from ARs.

The multi-method fusion algorithm proposed in this study also adheres to the aforementioned identification framework and integrates advanced strategies from multiple existing algorithms in its implementation. Designed for global-scale AR identification, the algorithm employs IVT as the detection variable, and in this study, the zonal and meridional IVT derived from ERA5 reanalysis are used as inputs, with a remapped horizontal resolution of $1° \times 1°$ to save storage and to facilitate computation. The algorithm consists of four steps, which are elaborated in detail below.

https://doi.org/10.5194/essd-2025-836
Preprint. Discussion started: 18 March 2026

2.1 Step 1: Extract an AR candidate from the IVT background field

At the specified time *t*, within the IVT background field, all grids where IVT exceeds the corresponding IVT intensity threshold are identified and marked. Starting from any unvisited marked grid (i.e., a grid that has been marked but not yet incorporated into any AR candidate), the algorithm recursively searches the eight neighboring grids for unvisited marked grids. This process continues iteratively until no new unvisited marked grids are found in the neighborhood, and resulting visited marked grids collectively form a continuous region as an AR candidate. Continuous regions that span the circular longitudinal boundary (connecting 360° back to 0°) artificially imposed in the data will be considered as a single AR candidate. Subsequent extraction of AR candidates starts from new unvisited marked grids and repeats the above procedure. When all marked grids on the IVT background field have been visited, the AR identification for this time step is deemed complete.

The identification algorithm employs the spatiotemporal quantile method proposed by Guan and Waliser (2024) to construct the IVT threshold field. Specifically, for the IVT threshold at time *t*, a 5-month window centered around the calendar month of *t* is defined, with a time interval of 6 hours (0000, 0600, 1200, 1800 UTC). The 85th percentile IVT value during this window, calculated over the period from 1980 to 2019, is used as the climatological base threshold for each grid globally. This 85th percentile criterion is selected empirically, based on the statistical results of ARs in existing studies (Guan and Waliser, 2015; Lavers et al., 2012). However, given that the thresholds are generally low in regions with climatologically low moisture content, which makes it difficult to effectively extract AR candidates, the algorithm also introduces hemispheric threshold lower limits: for each calendar month, the base threshold of grids where the area-weighted cumulative values reach the 5th percentile in the Northern and Southern Hemisphere are respectively adopted as the lower threshold limits for all grids within each hemisphere. This 5th percentile approximates the areal proportion of polar and other low-moisture regions, representing the base threshold at the margins of these regions and thereby enhancing the extraction of AR candidates within them. Compared to conventional fixed threshold lower limits, this hemispheric lower limit considers inter-hemispheric and seasonal variations in IVT, and its values are more consistent with thresholds used in polar-specific AR identification algorithms (Francis et al., 2020). Further, because the hemispheric lower limit dynamically adjusts in response to the base threshold, their combination forms a universally applicable global threshold-setting method suitable for various detection variables. Figure 1 illustrates the resulting IVT fields after merging the 85th percentile base threshold with the hemispheric threshold lower limit for each calendar month. This set of threshold fields, also denoted as the Level-0 threshold fields, will be described in detail in Step 4.

https://doi.org/10.5194/essd-2025-836
Preprint. Discussion started: 18 March 2026

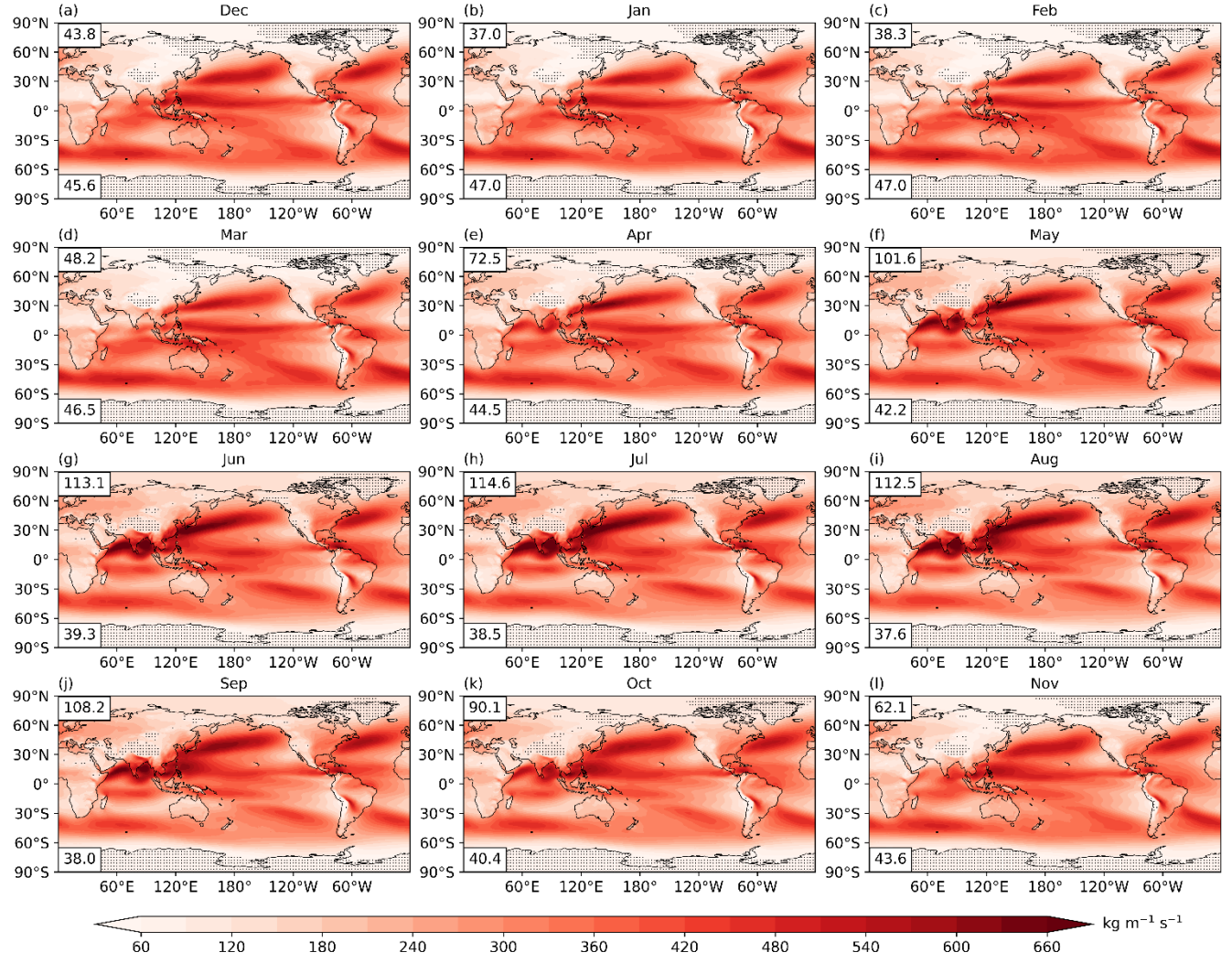

Figure 1. Climatological IVT threshold fields for each calendar month during 1980–2019. Shadings indicate the final threshold magnitude (units: kg m^{-1} s^{-1}) obtained after combining the 85th percentile value with the corresponding hemispheric lower limit. The lower limit values (units: kg m^{-1} s^{-1}) for the Northern and Southern Hemispheres are annotated in the upper-left and lower-left, respectively. The dotted areas denote grids where the threshold is fixed at the hemispheric lower limit.

2.2 Step 2: Identify the axis of the AR candidate

Accurately and robustly quantifying the key characteristics of AR candidates remains one of the central challenges in current AR identification. Existing algorithms typically construct a single characteristic axis along the core region of a candidate to capture its dominant trajectory, which is subsequently used to quantify its key characteristics. This study proposes to define two distinct characteristic axes for each AR candidate using two complementary methods with different emphases, thereby enabling a more comprehensive assessment of its relevant characteristics. One way to define AR characteristic axis is to connect local maxima in IVT. This approach is computationally efficient but sensitive to small-scale change. The other way is

https://doi.org/10.5194/essd-2025-836
Preprint. Discussion started: 18 March 2026


Open Access Earth System Science Data Discussions

to connect the centroids of IVT. This approach ensures a smoother and more stable AR track but often neglect small-scale change. In this study, two characteristic axes, derived from the two different approaches following Brands et al. (2017) and Pan and Lu (2019), are referred to as $Axis_1$ and $Axis_2$, respectively. Overviews of the two axes are provided below.

$Axis_1$. The axis generation begins at the grid with the maximum IVT value within the AR candidate. For the axis point, the surrounding 360° is divided into eight 45° sectors corresponding to the cardinal directions (N, NE, E, SE, S, SW, W, NW), each encompassing the adjacent grid in the direction. Within the sector aligned with the IVT direction at the axis point and its two neighboring sectors, the grid with the maximum IVT value among the three adjacent grids is selected as the next axis point. This iterative process continues downstream until the axis reaches the boundary of the AR candidate or the number of axis points exceeds 500, which prevents infinite looping in regions of strong vorticity. The upstream extension of $Axis_1$ follows the same procedure, except that the sectors are determined based on the opposite IVT direction.

$Axis_2$. The grid with the maximum IVT value within the AR candidate is selected as the initial reference point, serving to anchor the axis point. Around this reference point, a local region is defined by selecting the n nearest neighboring grids within the AR candidate, where n is set to 15% of the total number of grids in the candidate. The weighted average IVT direction at the reference point is calculated based on the distances of these grids from the reference point, and the line perpendicular to this direction is defined as the cross-section of the local region. The grids within the local region are then projected onto this cross-section, and their weighted center position is calculated based on both the distance from the reference point and the IVT magnitude, which is designated as the axis point corresponding to the reference point. Subsequently, the local region and weighted average IVT direction at the axis point are recalculated, and the axis point advances 100 km forward (backward) along the weighted IVT direction to obtain the next downstream (upstream) reference point. This iterative procedure continues downstream (upstream) to construct $Axis_2$, terminating when more than 90% of the grids in a local region are located behind (ahead of) the corresponding cross-section or the number of axis points exceeds 500.

https://doi.org/10.5194/essd-2025-836
Preprint. Discussion started: 18 March 2026

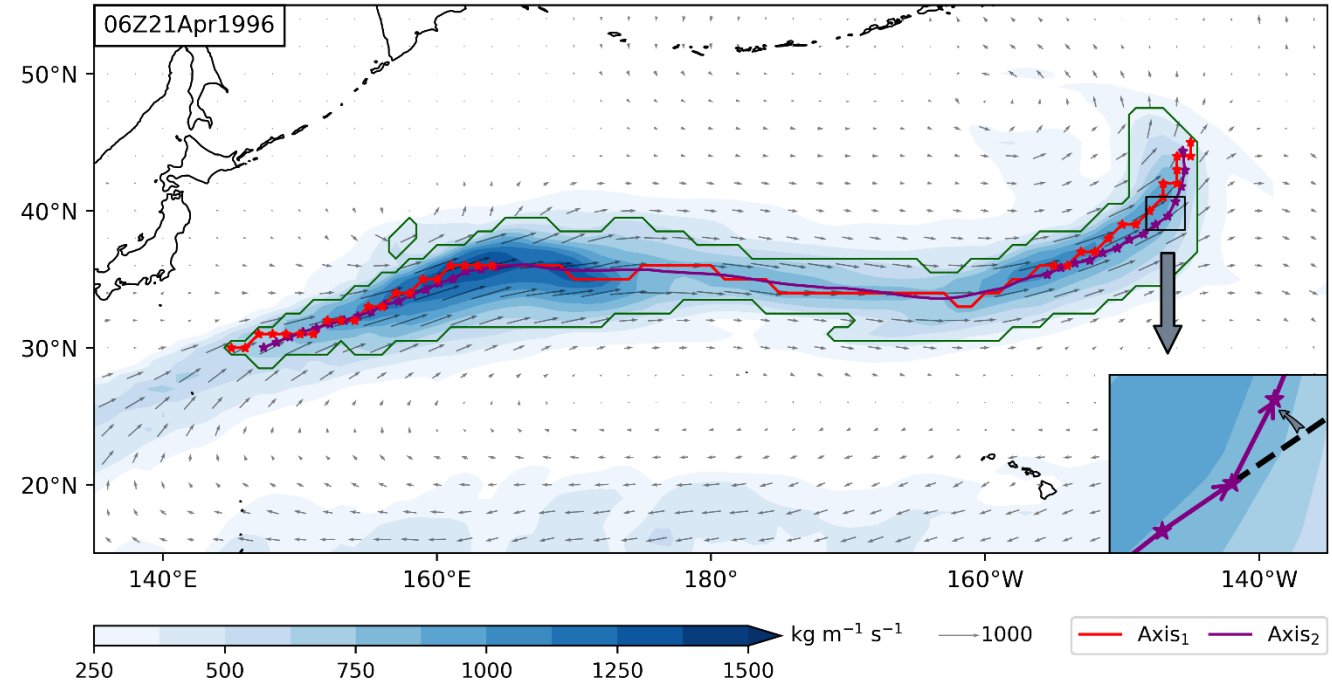

Figure 2. An example illustrating the quantification of main characteristics of an AR candidate. It shows the shape boundary of the candidate (solid green curve), $Axis_1$ (solid red curve), and $Axis_2$ (solid purple curve). Stars in corresponding colors mark the points on each axis where the ratio of the poleward component to the IVT intensity exceeds 0.25, and consecutive marked points form continuous segments. The lower-right inset provides an enlarged view of the region within the black box, highlighting the turning angle between adjacent vectors formed by axis points. Shading indicates IVT magnitude (units: kg m^{-1} s^{-1}), and vectors denote the IVT direction.

On the one hand, the elongated and narrow morphology of ARs serves as a key distinguishing feature from other moisture-rich weather systems. On the other hand, as a critical pathway for global meridional water vapor transport, ARs are associated with poleward-directed moisture flux that should be accounted for in their identification. Therefore, this study mainly considers the characteristics of AR candidates in these two aspects, with most diagnostic metrics being quantified based on their characteristic axes. Figure 2 illustrates an example of an AR candidate, along with its $Axis_1$ and $Axis_2$. For either axis, the sum of the geographical distances between consecutive axis points is defined as the length of the AR candidate. The equivalent width is then derived as the ratio of the geographic area of the candidate to its length.

To characterize the curvature of the AR candidate, two metrics are employed: the sum of turning angles along the axis (Pan and Lu, 2019) and the straightness ratio of the axis. The sum of turning angles is computed as follows: each pair of adjacent axis points forms a vector pointing downstream; starting from the first vector at the upstream end, the turning angle between the current vector and the next adjacent vector is calculated sequentially (Fig. 2) and cumulatively summed, with counterclockwise angles assigned positive values. The straightness ratio is defined as the ratio of the great-circle distance between the axis endpoints to the total axis length.

https://doi.org/10.5194/essd-2025-836
Preprint. Discussion started: 18 March 2026

To quantify the poleward water vapor transport characteristic of the candidate, the algorithm computes the total length of axis segments satisfying the poleward moisture flux condition (Guan and Waliser, 2024). Each segment consists of consecutive axis points where the ratio of the poleward component of IVT to the total IVT intensity exceeds 0.25, as marked with stars in Fig. 2. This metric provides a quantitative assessment of the potential poleward water vapor transport structures within the AR candidate. It should be noted that both Axis_1 and Axis_2 yield separate sets of the aforementioned metrics, enabling a comprehensive diagnostic assessment of the corresponding characteristics of the AR candidate.

2.3 Step 3: Diagnose the AR candidate

In the diagnostic assessment based on morphological features, the AR candidate will be excluded if it fails to satisfy all of the following criteria: 1) At least one axis has a length exceeding 2000 km; 2) At least one axis exhibits a length-width ratio greater than 2; 3) For each axis, the sum of turning angles is less than $300° - i \times 30°$, and the standard deviation of the two sums is less than 60°, where $i \in \{0, 1, 2, 3, 4\}$ denotes the current threshold-level index within the threshold adjustment step, as detailed in the next step; 4) For each axis, the straightness ratio exceeds $0.85 - l/10000$, where l denotes the axis length. The first two criteria are geometric constraints based on statistical studies of ARs, and are designed to ensure the AR candidate exhibits elongated and narrow morphology. The latter two criteria are curvature constraints derived from extensive visual inspection and sensitivity tests, and are designed to effectively filter out highly curved moisture transport systems, particularly tropical cyclones. Specifically, the third criterion is based on the sum of turning angles along the axis, which can more directly quantify and diagnose the curvature characteristics of candidates at different scales, offering broad applicability and stability. The fourth criterion serves as a supplementary filter, primarily targeting a few high-curvature AR candidates with incomplete structures extracted by IVT threshold (Fig. 3a). Although such cases are rare, they are difficult to completely avoid in all threshold-based identification algorithms. When structural incompleteness prevents such candidates from being filtered out by the third criterion, the fourth criterion detects their low straightness ratios of the axes and accordingly excludes them. Notably, this criterion incorporates scale dependence, enhancing its sensitivity to small-scale candidates, which are the most common in such special cases.

https://doi.org/10.5194/essd-2025-836
Preprint. Discussion started: 18 March 2026

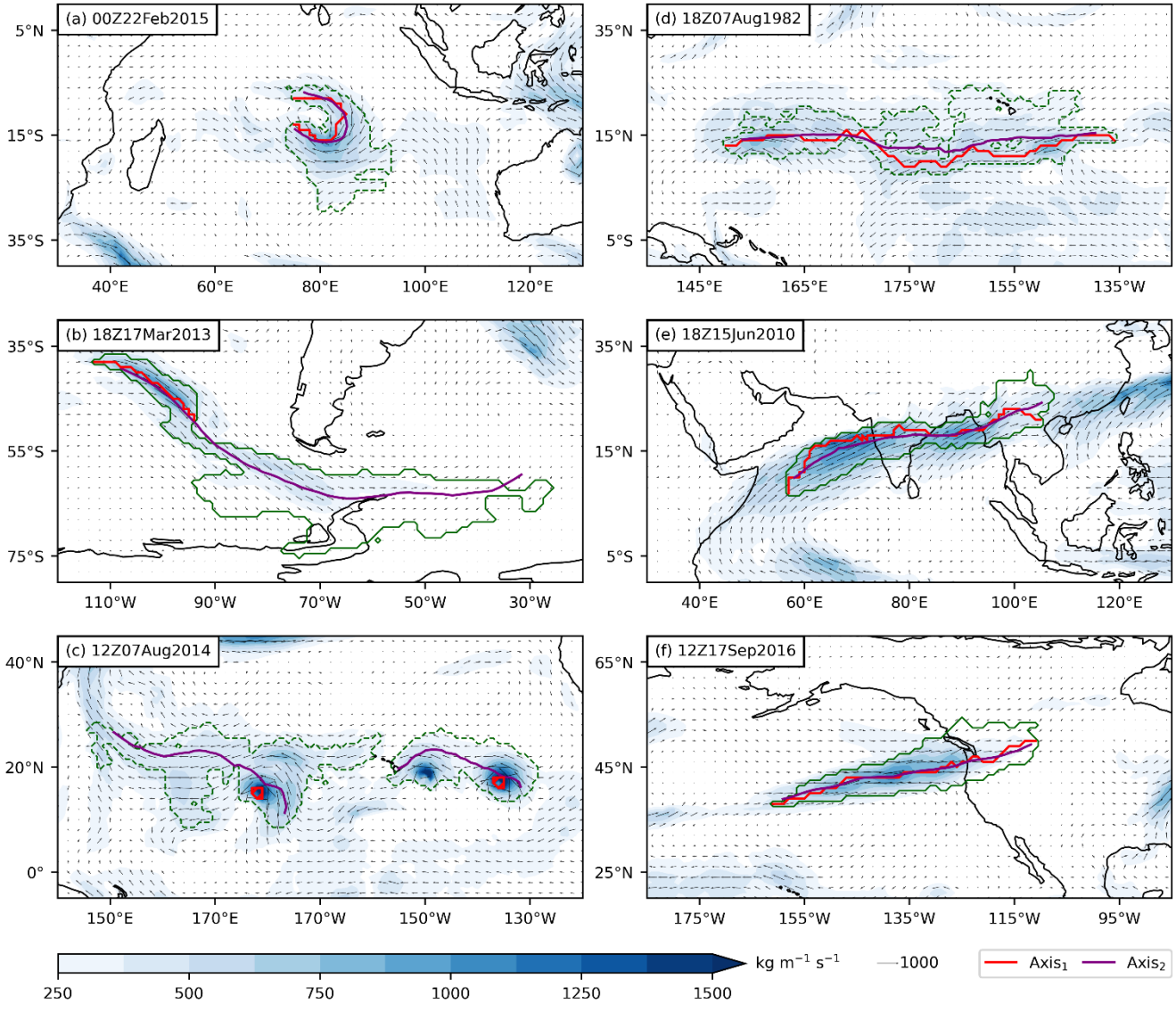

Figure 3. Examples of AR candidates. The shape boundaries of candidates are marked by green curves (solid green curves indicate AR activities, while dashed green curves are non-ARs, excluded from our algorithm). $Axis_1$ is shown in solid red curve, and $Axis_2$ is shown in solid purple curve. The IVT is shown in vectors with the intensity shaded (units: kg m^{-1} s^{-1}).

It is worth emphasizing that the dual-axis collaborative representation proposed in this algorithm exhibits unique advantages in characterizing the morphological features of AR candidates and related diagnostic assessments. Each of the two axes ($Axis_1$ versus $Axis_2$) has its own strengths and limitations when independently representing the morphological characteristics of AR candidates. $Axis_1$, whose trajectory is determined by dynamically selecting the maximum IVT value immediately around each grid, offers high computational efficiency and sensitivity to local turbulent disturbances. This enables it to respond effectively to small-scale changes but may also lead to premature termination of the axis finding process due to preset boundary conditions

https://doi.org/10.5194/essd-2025-836
Preprint. Discussion started: 18 March 2026

(Fig. 3b). In contrast, $Axis_2$ is the connection line of the centroids of each part of the AR candidate constructed based on the K-nearest neighbors and local weighted regression, which ensures a smoother and more stable axis but may overlook some smaller vortex systems (Fig. 3c). To overcome the respective disadvantage of the two methods, our algorithm integrates both methods and refines the diagnostic logics. Namely, the former method can more accurately capture small-scale disturbances than the latter. However, the latter can correct unrealistic path diversions, which prevail in the former method due to local vortices. Conceptually, the axis definitions in Guan and Waliser (2015, 2024) have elements similar to $Axis_1$. A dual-method axis identification strategy here is expected to enhance the robustness of AR identification in complex weather conditions, particularly to have a better representation of AR systems with multi-core structures or irregular shapes.

The poleward water vapor transport characteristics of AR candidates can reflect their potential dynamical linkages with weather systems across multiple scales. The diagnostic assessment of these characteristics aims to exclude candidates exhibiting pronounced zonal features, such as tropical moisture filaments and water vapor transport belts in the mid- and high-latitudes that are almost entirely controlled by prevailing winds. Drawing upon established screening criteria from prior algorithms (Pan and Lu, 2020; Guan and Waliser, 2024), the AR candidate will be excluded if it fails to satisfy all of the following criteria: 1) The fraction of grids within the 20° S–20° N latitude band must not exceed 95%; additionally, if this fraction exceeds 50%, then the proportion of grids where the angle between the IVT direction and the latitude circle is less than 15° must not exceed 50%; 2) There must be at least one axis with a total length of segments exhibiting poleward water vapor transport characteristics that exceeds 800 km, or at least one axis whose length exceeds $3500 - R_p \times 5000$ km, where R_p is required to be greater than 0 and is defined as the ratio of the area-weighted average of the poleward IVT component to the area-weighted average of total IVT magnitude. The first criterion can effectively eliminate zonally-oriented tropical moisture filaments (Fig. 3d), while retaining water vapor transport corridors in the tropics that exhibit characteristics consistent with ARs, such as the strong water vapor transport belts embedded in the East Asian summer monsoon circulation (Kamae et al., 2017; Yang et al., 2018; Fig. 3e) and the tropical moisture exports over the North Pacific (Knippertz and Wernli, 2010). The second criterion is primarily designed for mid- and high-latitude candidates, emphasizing the presence of internal poleward-directed moisture transport structures rather than imposing a rigid threshold on the poleward IVT component, thereby effectively avoiding the erroneous exclusion of some ARs with an overall zonally-oriented extension (Fig. 2). Additionally, the second half of this criterion takes into account the possibility that the poleward water vapor transport along the axes of a few ARs may be locally weak (Fig. 3f), and it comprehensively assesses the overall poleward moisture transport characteristics of the candidate by incorporating its spatial scale as a supplement. As with the morphological criteria, the specific parameter thresholds in these criteria are based on prior research, combined with extensive visual inspection and sensitivity tests.

When the AR candidate satisfies all the above criteria, the algorithm identifies it as an AR and archives the associated data. Subsequently, a new AR candidate is extracted from the IVT background field in Step 1, and its main characteristics are quantified and diagnosed following the same procedure. If the candidate is excluded due to failing to meet the criteria, the algorithm performs an additional verification of the corresponding region through the threshold adjustment step in the next step.

https://doi.org/10.5194/essd-2025-836
Preprint. Discussion started: 18 March 2026

2.4 Step 4: Re-check the excluded AR candidate

For an initially excluded AR candidate, the algorithm employs a threshold adjustment step to re-check if water vapor transport structure is consistent with AR characteristics in the interior of the corresponding region, as proposed by Guan et al. (2018). Specifically, based on the Level-0 IVT threshold fields at the 85th percentile combined with the hemispheric threshold lower limit (see Step 1), the algorithm additionally establishes four sets of ascending threshold fields, corresponding to the combinations of the 87.5th, 90th, 92.5th, and 95th percentile base thresholds, denoted as Level-1 to Level-4 in the threshold adjustment step. For an AR candidate initially excluded, the IVT values of each grid within the region are compared against the corresponding thresholds in the Level-1 threshold field. Grids with IVT values exceeding this threshold are re-registered as unvisited marked grids in the IVT background field, and retained for extraction as the potential new AR candidate in Step 1. Concurrently, the algorithm records the threshold-level index of the threshold field used to extract the current candidate. If the candidate fails to satisfy the diagnostic criteria, the procedure is repeated using the threshold field of the next level. If a candidate extracted from the Level-4 threshold field still does not meet the criteria, the verification process for that region is concluded.

The threshold adjustment step modifies the IVT threshold to regulate the spatial extent of AR candidates, with two primary functions. First, for some overly broad AR candidates that fail to meet the length-width ratio criterion, their core regions obtained after spatial contraction may satisfy the criterion. This scenario predominantly occurs over moisture-rich oceanic regions, where broad candidates with loose peripheral structures are more likely to be extracted. Second, certain AR candidates may consist of multiple water vapor transport systems. When merged candidates exhibit clear discontinuities in water vapor transport, the threshold adjustment step enables their separation. For example, Fig. 4a illustrates an AR candidate initially extracted based on the Level-0 IVT threshold field, which would be excluded due to its failure to meet the diagnostic criterion based on the curvature metric derived from the sum of turning angles. Through the threshold adjustment step, the constituent tropical cyclone and AR are separated, thereby preventing the erroneous removal of the latter. Furthermore, this step also alters the curvature metric of the tropical cyclone component due to changes in the region (Fig. 4b). If the original criterion was still applied, it might be incorrectly retained. Therefore, the algorithm dynamically adjusts the relevant criterion based on the current IVT threshold-level index. In fact, the aforementioned two scenarios are inherent limitations of using threshold to extract AR candidates, but these can be effectively improved by incorporating a threshold adjustment step.

https://doi.org/10.5194/essd-2025-836
Preprint. Discussion started: 18 March 2026

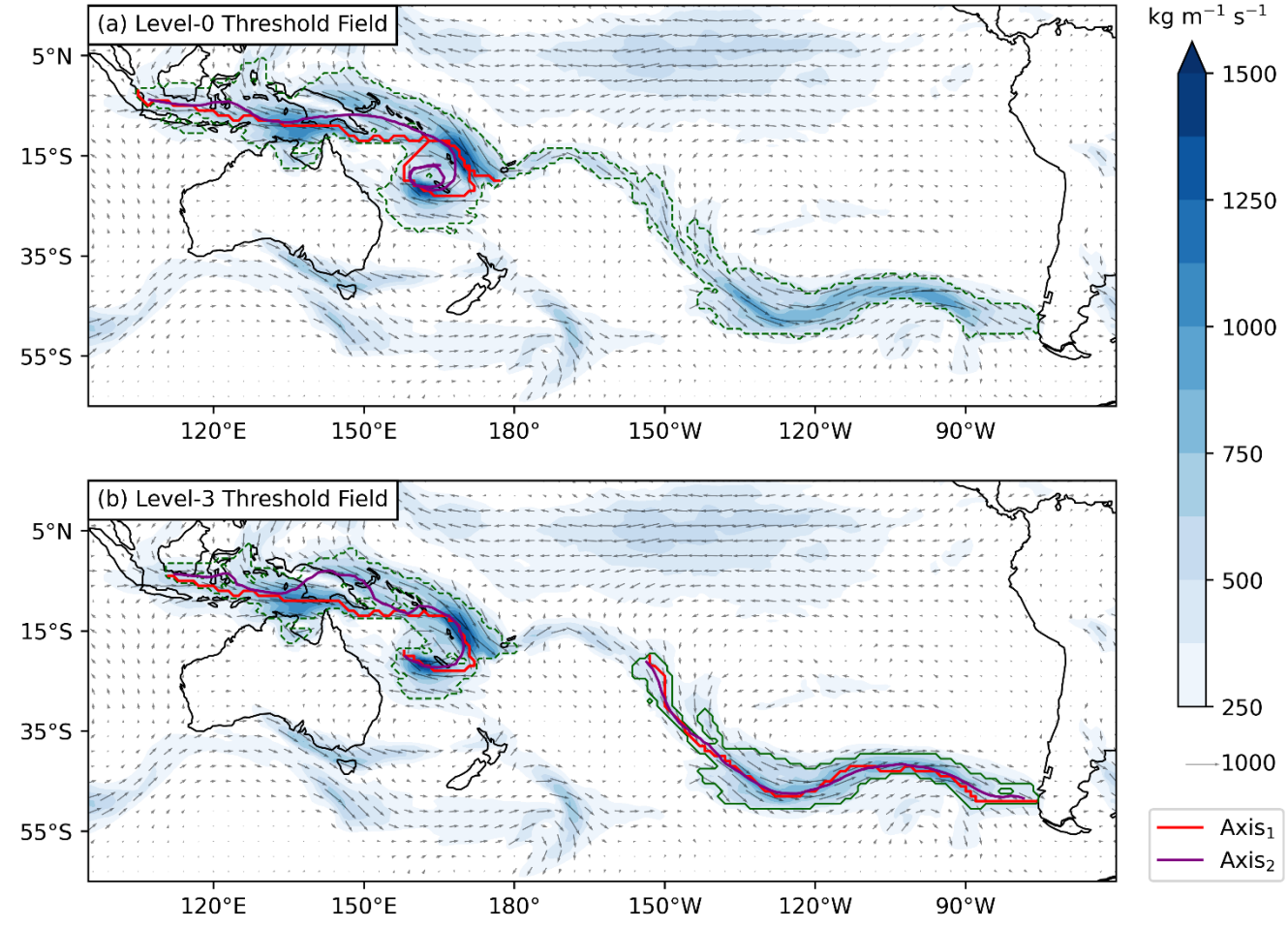

Figure 4. An example of the threshold adjustment step applied in the algorithm at 12:00, 8 January 1979. (a) AR candidate extracted using the Level-0 threshold field. (b) AR candidates extracted using the Level-3 threshold field. The shape boundaries of candidates are marked by green curves (solid green curves indicate AR activities and dashed green curves non-ARs). $Axis_1$ is shown in solid red curve, and $Axis_2$ is shown in solid purple curve. The IVT is shown in vectors with the intensity shaded (units: kg m^{-1} s^{-1}).

3 Data and application

3.1 Comparisons with existing databases

This study employed the IVT dataset derived from ERA5 reanalysis data as input, with a remapped horizontal resolution of 1° × 1° at a time interval of 6 hours (0000, 0600, 1200, 1800 UTC). Applying the aforementioned AR identification algorithm, a global AR database spanning from 1940 to 2024 with a 6-hour time interval is constructed. The database is constructed as a three-dimensional spatiotemporal array that records AR occurrences on a two-dimensional grid for each timestep. At every timestep, individual ARs are sequentially assigned an integer label starting from 1, which are mapped onto the corresponding grids within their occurrence regions, while non-AR regions are assigned a value of 0. The combination of timestamp and

https://doi.org/10.5194/essd-2025-836
Preprint. Discussion started: 18 March 2026

integer label provides a unique identifier for each AR, facilitating the direct extraction of data for individual ARs in practical applications, as well as further tracking of their complete life cycles by analyzing spatial overlaps between consecutive timesteps (Zhou et al., 2018).

To evaluate the performance of the algorithm and the AR database (hereinafter referred to as DB1) it constructed, this study conducted a comparative analysis between DB1 and two existing global AR databases (hereinafter referred to as DB2 and DB3). DB2 was developed by Guan and Waliser (2024) using the Tracking Atmospheric Rivers Globally as Elongated Targets (tARget) algorithm with ERA5-derived IVT data as input; this algorithm has been comprehensively evaluated in previous studies and provides a critical reference for the IVT threshold setting in our algorithm. DB3 was generated by Wang et al. (2024) through a data fusion algorithm integrating 12 independently produced AR databases, offering broad representativeness. A common period from 1980 to 2016 is selected for analysis, during which the total number of ARs and their latitudinal distribution are calculated for all three databases. The number of ARs refers to the cumulative AR snap counts across all timesteps (0000, 0600, 1200, 1800 UTC), and the location of each AR is determined based on its area distribution in different latitude bands. This study further quantifies the number of ARs identified consistently in DB1 and DB2 (DB3). Specifically, for each AR in DB1, the longer axis ($Axis_1$ versus $Axis_2$) is mapped onto the grid of the same timestep in DB2 (DB3). If more than 1000 km of the axis lies within an AR region in the target database, these two ARs are considered consistent. This criterion is designed to assess spatial overlap in core structural regions, ensuring both computational efficiency and robustness. As shown in Table 1, all three databases exhibit consistent spatial patterns, indicating that ARs predominantly occur in the mid-latitudes, with higher frequency observed in the Southern Hemisphere than in the Northern Hemisphere. However, discrepancies exist in the absolute counts across different databases. Overall, the counts in DB1 and DB2 are comparable and exceed those in DB3. In terms of identification agreement, DB1 captures the majority of ARs present in DB2 and DB3, achieving the highest consistency rate in the mid-latitudes despite the largest sample size there.

Table 1. Distribution of AR counts and identification consistency across three databases from 1980–2016. Comparisons are performed separately for low- (0°–30°), mid- (30°–60°), and high-latitude (60°–90°) regions. Values in parentheses indicate the number of ARs in DB1 that are consistently identified in DB2 and DB3, respectively.

Regions	Num of ARs in DB1	Num of ARs in DB2		Num of ARs in DB3	
90° N–60° N	61090	64698	(55215)	10036	(8565)
60° N–30° N	196067	189985	(172840)	137952	(123898)
30° N–0°	53209	70697	(44488)	25214	(19089)
0°–30° S	54258	70800	(47659)	27422	(22162)
30° S–60° S	239178	233682	(218624)	208835	(192036)
60° S–90° S	56569	61002	(52180)	5838	(4519)

https://doi.org/10.5194/essd-2025-836
Preprint. Discussion started: 18 March 2026

Global	660371	690864	(591006)	415297	(370269)

To further evaluate the potential differences in ARs among DB1, DB2, and DB3, as well as the characteristics of AR frequency distribution in DB1, this study separately calculated the occurrence frequencies of ARs in all three databases during the period from 1980 to 2016 for the northern wintertime (November to March), northern summertime (May to September), and the entire year. The occurrence frequency at each grid is determined by dividing the number of time steps identified with ARs by the total number of time steps. Figure 5a–c shows the spatial distribution of AR frequency in DB1 for wintertime and summertime, respectively. ARs exhibit the highest occurrence frequency in mid-latitude ocean basins, possibly due to frequent extratropical storms and relatively abundant moistures (Eiras-Barca et al., 2018; Guan and Waliser, 2019). Further, the initial activity positions are usually located closer to the equator in the wintertime hemisphere and farther poleward in the summertime hemisphere. This spatial pattern and seasonal evolution of AR frequency distribution is highly consistent with storm tracks (Bengtsson et al., 2006; Priestley and Catto, 2022). Specifically, ARs exhibit a southwest-northeast direction under the background of the Northern Hemisphere westerly circulation. Therefore, ARs have a more direct and intuitive impact on the west coasts of the continents especially in the northern winter (Lavers and Villarini, 2015; Mahoney et al., 2016). Notably, seasonal expansion of the Western North Pacific Subtropical High (WNPSH) builds a moisture transport pathway over East Asia (Kwon et al., 2024; Park et al., 2021). Figure 5d–i illustrates the differences in AR occurrence frequency between DB1 and DB2, and between DB1 and DB3. The discrepancies between DB1 and DB2 are mainly evident in tropical and mid-latitude regions: DB1 shows slightly lower frequency in the tropics but slightly higher frequency in the mid-latitudes compared to DB2. Relative to DB3, DB1 exhibits higher frequency over continents and high-latitude regions, which are typically characterized by low moisture content, while showing close agreement in the tropics and in mid-latitude ocean basins where ARs are most active.

https://doi.org/10.5194/essd-2025-836
Preprint. Discussion started: 18 March 2026

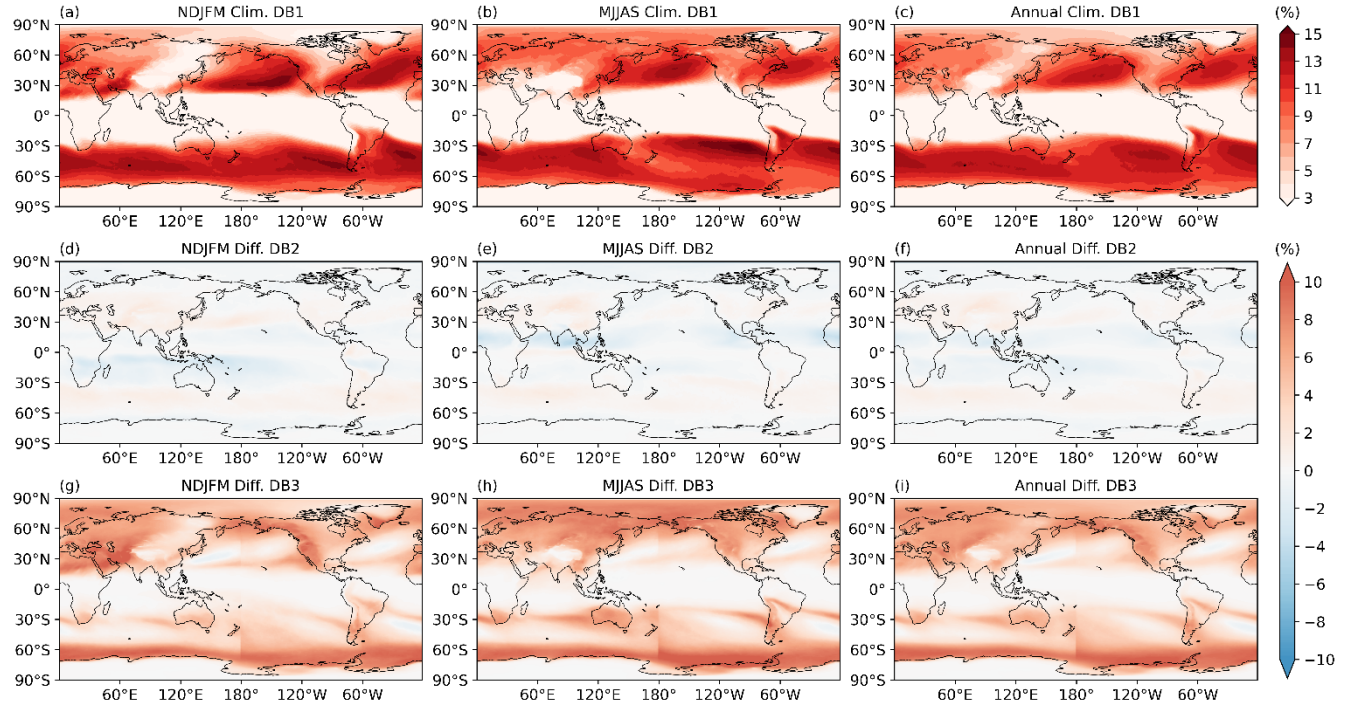

Figure 5. Global distribution of AR occurrence frequency using the present algorithm (DB1) for (a) the northern wintertime, (b) northern summertime, and (c) annual mean based on ERA5 from 1980–2016. (d–i) As in (a–c) but for the frequency differences between DB1 and DB2 (d–f) and between DB1 and DB3 (g–i).

The discrepancies in AR identification across the three databases arise from multiple factors. A critical determinant is the threshold applied to the intensity of the detection variable within the algorithms, particularly its lower limit, which governs the number of ARs identified in lower-moisture regions. The global AR databases fused in DB3 are based on a fixed threshold lower limit, which is generally higher than the hemispheric lower limit used in DB1 and DB2. Consequently, DB3 identifies significantly fewer ARs in low-moisture continental and high-latitude regions. In contrast, over mid-latitude ocean basins where moisture is abundant and AR activity is frequent, the magnitudes of thresholds across the respective algorithms are comparable, resulting in minimal differences in AR counts among the databases. The discrepancies between DB1 and DB2 mainly stem from differing diagnostic criteria for the poleward water vapor transport characteristics of AR candidates. The algorithm used in this study applies stricter filtering of tropical moisture filaments, leading to fewer identified ARs in tropical regions in DB1 than DB2. Conversely, in the mid-latitudes, the algorithm adopts less strict criteria for zonally-oriented ARs, yielding a slightly higher AR count in DB1. Furthermore, variations exist across algorithms in the quantification methods and diagnostic criteria for the morphological characteristics of candidates, as well as in the spatial resolution of input data. These technical differences all affect the specific AR identification results; for instance, DB1 excludes the AR candidates shown in Fig. 3a, c and 3d while retaining the candidate in Fig. 3f, compared to other databases.

https://doi.org/10.5194/essd-2025-836
Preprint. Discussion started: 18 March 2026

3.2 Case analysis for typical weather extremes

To assess the feasibility of DB1 in tracking the complete life cycle of ARs and to further understand the dynamic evolution characteristics, this study selects two weather extreme events with broad impacts for case analysis. The first case is the East Asian Meiyu rainfalls in late June 2018, which successively affected eastern China, the Korean Peninsula, and Japan, with extreme precipitation triggering severe disasters in wide areas of East Asia (Tsuguti et al., 2019). The second case is the Australian forest wildfires in late January 2020 (Black Summer), when the wildfires were gradually brought under control and were followed by persistent precipitation in early February, leading to multiple cascading hazards (Kemter et al., 2021).

The Meiyu is a seasonal rainy period that occurs as the East Asian summer monsoon advances northward into the subtropical region of East Asia, typically during June and July (Ding et al., 2020). The Meiyu season is characterized by persistent precipitation, and Wang et al. (2021) showed that AR is an important component of Meiyu system, exerting significant impacts on Meiyu rainfalls. In late June 2018, the Meiyu rainfalls were influenced by interactions of multi-scale weather systems, including the WNPSH, extratropical cyclone, and Typhoon Prapiroon, exhibiting a long duration and high precipitation intensity. Figure 6 illustrates the evolution of the AR during this period. Initially, the AR was embedded within the monsoon flow and extended along the WNPSH edge in a northeast-southwest orientation, continuously transporting the warm, moist air northward from the Bay of Bengal, the South China Sea, and western Pacific (Fig. 6a). As the extratropical cyclone located northwest of the AR downstream slowly moved eastward, its trailing cold air mass advanced southward and converged with the warm, moist airflow in the central region of the AR, generating a low-level cyclonic shear. This interaction intensified moisture convergence and strengthened moisture transport in the midsection of the AR; as the cyclone continued moving eastward, the water vapor transport was enhanced and shifted downstream (Fig. 6b, c). Concurrently, Typhoon Prapiroon in the south developed and moved poleward, while the WNPSH gradually shifted northward, guiding the AR to reorient into an east-west direction. Subsequently, as the extratropical cyclone moved offshore, its influence on the AR diminished. The AR stabilized along the northwestern periphery of the WNPSH (Fig. 6d, e), maintaining a quasi-stationary state until the mature Typhoon Prapiroon approached, disrupting the original circulation and terminating the AR (Fig. 6f). This process, combined with the subsequent typhoon landfall, contributed to the “Heavy Rain Event of July 2018” in Japan (Sayama et al., 2020). In summary, this AR was primarily governed by the WNPSH and modulated by both the extratropical cyclone and the typhoon, exhibiting pronounced quasi-stationary feature that distinguishes it from typical ARs. Figure 6 also presents the AR identification results from DS2. While generally consistent with DS1, discrepancies are evident in Fig. 6a, f. Specifically, no AR is identified in DS2 in Fig. 6a. In Fig. 6f, the AR identified in DS2 includes the southern Typhoon Prapiroon, whereas the result in DS1 excludes it; this distinction arises because the $Axis_1$ used in DS1 effectively captures the internal vortex structure, enabling its separation from the AR through the threshold adjustment step.

https://doi.org/10.5194/essd-2025-836
Preprint. Discussion started: 18 March 2026

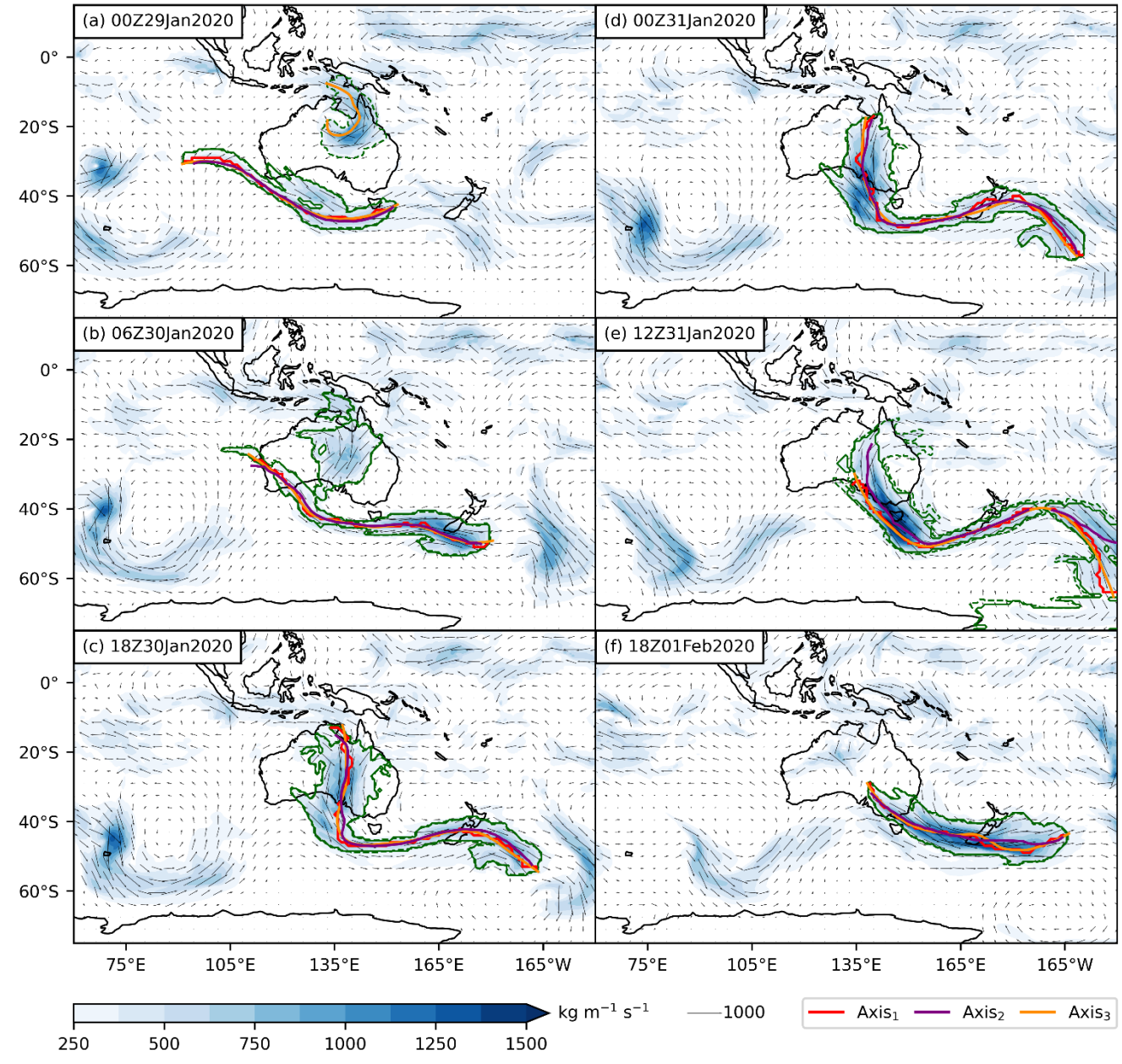

Figure 6. The evolutions of the AR during the Meiyu period in June 2018. (a–f) Six snapped instances from 06:00, 25 June to 18:00, 30 June 2018 with an uneven time interval of 24, 30, 24, 30 and 24 hours, respectively (marked in the upper-left for each snap). The solid green curve shows the AR boundary in DB1, and dashed green curve shows that in DB2. $Axis_1$ (solid red curve) and $Axis_2$ (solid purple curve) are the two AR axes in DB1, and $Axis_3$ (solid orange curve) is the AR axis in DB2. The IVT is shown in vectors with the intensity shaded (units: kg m^{-1} s^{-1}).

Australia is a typical monsoon-controlled region, and Asian and Australian monsoon is usually viewed as a unified system (Cheng et al., 2024). The weather and climate in the Asian and Australian monsoon-controlled regions are influenced by large-

https://doi.org/10.5194/essd-2025-836
Preprint. Discussion started: 18 March 2026

scale climate variability across various time scale (Lim et al., 2019; Risbey et al., 2009). During the 2019–2020 austral Black Summer, a series of uncontrollable forest wildfires broke out across Australia. The extreme drought occurred under the strong positive Indian Ocean Dipole (IOD) and the stratospheric disturbance was possibly an important contributing factor (Rao et al., 2020). In late January 2020, a well-developed AR traversed Australia, delivering substantial moist air that effectively suppressed the wildfires and creating conditions for extinguishing the wildfires. Figure 7 shows the evolution of the ARs in January 2020 for several snaps at the end of the Australian wildfire. Initially, a narrow, zonal AR was present over the southwestern seas of Australia, moving eastward at a relatively low speed, while a tropical cyclone was moving inland from northern Australia (Fig. 7a). Once landing, the tropical cyclone gradually weakened, and its residual circulation merged with the upstream portion of the AR, causing changes in the upstream circulation and forming a trough-ridge dipole system on both sides of the AR (Fig. 7b). Subsequently, a substantial amount of tropical moisture was transported along the AR, traversing Australia in a meridional direction (Fig. 7c, d). Concurrently, cold air from the southwest converged with poleward-flowing warm, moist tropical air on the western flank of the AR, where the cyclic shear zone developed, which in turn fed the upstream AR. Thereafter, the entire system continued to move eastward and left Australia; under the influence of a northern anticyclone, the AR reoriented into an east-west direction and persisted along its southern periphery (Fig. 7e, f). Overall, the most prominent feature of this AR is the direct influence from the tropical cyclone residual circulation, which led to deformation of the upstream circulation and the AR orientation. As a consequence, abundant moisture was transported across Australia and help to cease the uncontrollable wildfires that had lasted for months. Similar to Fig. 6, the AR identification results in Fig. 7 are largely consistent between DS1 and DS2, with the exception of Fig. 7a. In Fig. 7a, an AR is identified in DS2 within the northern tropical cyclone, whereas it is excluded in DS1; this exclusion is attributed to the diagnostic criterion for the axis straightness ratio employed in our algorithm, which effectively filters out such small-scale AR candidates with incomplete vortex structures.

https://doi.org/10.5194/essd-2025-836
Preprint. Discussion started: 18 March 2026

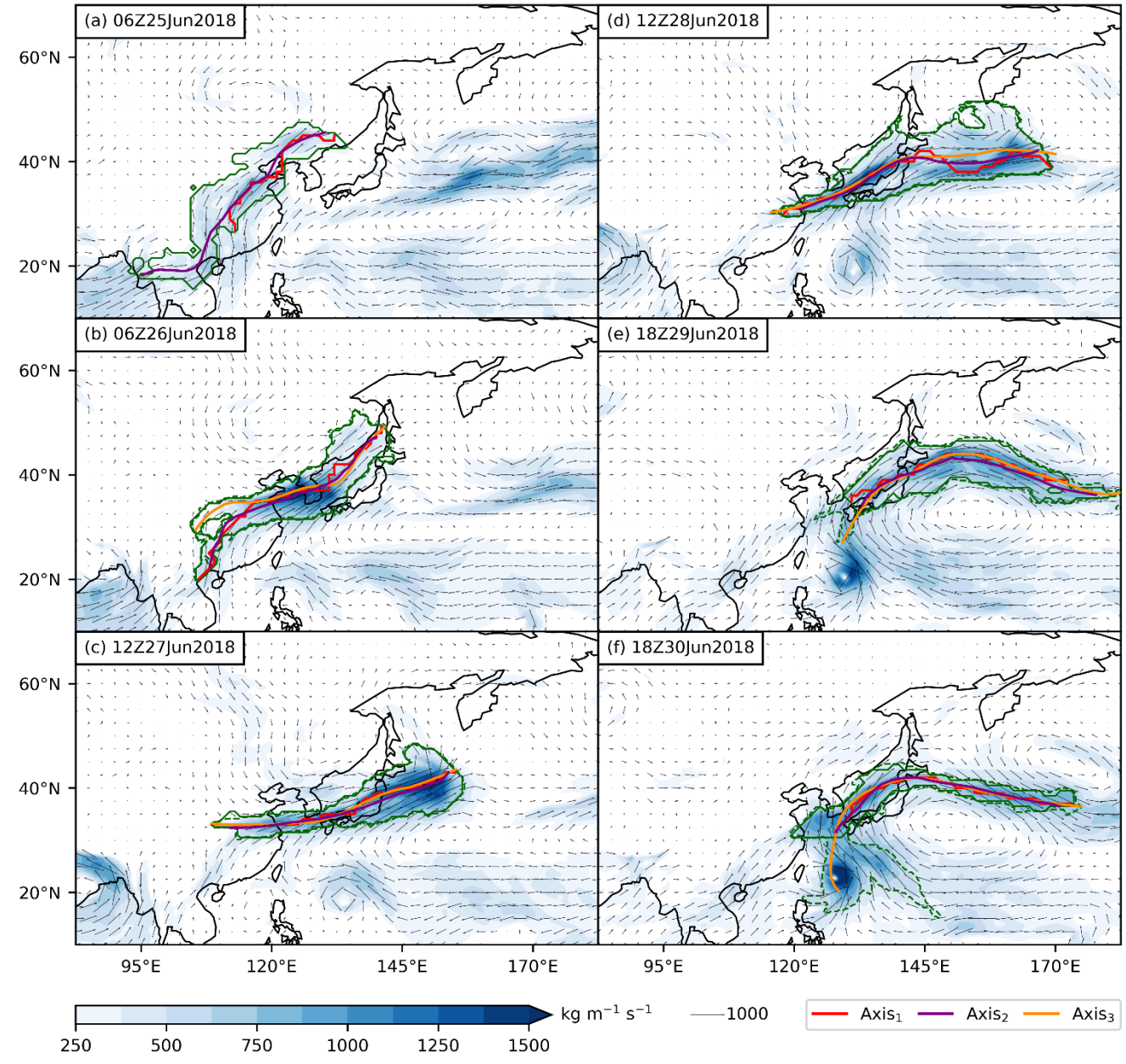

Figure 7. The evolutions of the AR during the 2019–2020 Australia wildfires in January 2020. (a–f) Six snapped instances from 00:00, 29 January to 18:00, 1 February 2020 with an uneven time interval of 30, 12, 6, 12 and 30 hours, respectively (marked in the upper-left for each snap). The solid green curve shows the AR boundary in DB1, and dashed green curve shows that in DB2. $Axis_1$ (solid red curve) and $Axis_2$ (solid purple curve) are the two AR axes in DB1, and $Axis_3$ (solid orange curve) is the AR axis in DB2. The IVT is shown in vectors with the intensity shaded (units: kg m^{-1} s^{-1}).

https://doi.org/10.5194/essd-2025-836
Preprint. Discussion started: 18 March 2026

4 Data availability

The AR database developed in this study, based on the multi-method fusion identification algorithm, is hosted on Zenodo at https://doi.org/10.5281/zenodo.18051602 (Chen and Rao, 2025). The zonal and meridional IVT data from ERA5 reanalysis can be accessed from the Copernicus Climate Data Store at https://cds.climate.copernicus.eu/. Additionally, the AR database based on the tARget version 4 algorithm by Guan and Waliser (2024) is available at https://dataverse.ucla.edu/dataverse/ar; the AR database developed using a data fusion algorithm by Wang et al. (2024) is available at https://zenodo.org/records/10229029.

5 Conclusion and discussion

This study proposes a fused algorithm for identifying ARs at specified times, using IVT as the detection variable and designed for global-scale applications. The algorithm builds upon the widely adopted objective conditional identification framework and consists of four steps: 1) Extracting an AR candidate from the IVT background field through the predefined threshold field; 2) Generating two distinct characteristic axes of the candidate using complementary methods and quantifying its key characteristics along these axes; 3) Conducting the comprehensive diagnostic assessment based on two independent sets of quantitative metrics to determine whether the candidate satisfies the criteria for an AR; 4) Verifying the region of the candidate if it fails to meet the prescribed criteria. The algorithm integrates advanced strategies from multiple existing identification algorithms across these steps. Furthermore, a dual-axis test method is introduced in steps 2) and 3), which enables more comprehensive quantification and diagnosis of AR characteristics, thereby enhancing the robustness of the identification process.

Using the ERA5 reanalysis dataset from 1980 to 2024 as inputs, this algorithm analyzes the IVT to produce an AR database covering the globe. A systematic evaluation is conducted by comparing this database with two recently published AR databases: Version 4 product from Guan and Waliser (2024) and the AR database from Wang et al. (2024). The comparison focuses on AR frequency, spatial distribution, and seasonal variability over the common period of 1980–2016, along with a discussion of potential sources of discrepancies. The results indicate a high degree of consistency among the databases in mid-latitude ocean basins, where AR activity is most frequent. The primary source of differences arises from the threshold applied to the detection variable in the identification algorithms, particularly over continental and high-latitude regions characterized by low moisture content. Additionally, algorithmic variations in the quantitative metrics and diagnostic criteria for the key characteristics of AR candidates also influence their identification.

The AR database using our algorithm shows prosperous application vista in the future weather and climate research. Two extremes are selected to illustrate the possible relationship between ARs and severe natural disasters, which had significant societal, economic, and ecological impacts. One of those cases is the East Asian Meiyu rainfalls in late June 2018, during which the AR was constrained by the WNPSH and exhibited pronounced quasi-stationary characteristics. The other is the cessation of the Black Summer in Australia in late January 2020 after a long-lasting wildfire, when the AR was directly

https://doi.org/10.5194/essd-2025-836
Preprint. Discussion started: 18 March 2026

influenced by the tropical cyclone residual circulation, leading to a marked deformation of its circulation structure. It is revealed that the AR evolutions were influenced by distinct weather systems during those extremes, exhibiting undetectable characteristics that differ from typical ARs associated with extratropical cyclones. These non-canonical cases provide valuable insights into the diversity of ARs, which show possible applications outlooks for the forecasts of related weather and climate extremes in the future.

Author contributions

All authors participated in the database generation and analysis. HC and JR were responsible for the original draft preparation. All authors contributed to the review and editing of the final manuscript.

Competing interests

The contract author has declared that none of the authors has any competing interests.

Disclaimer

Publisher's note: Copernicus Publications remains neutral with regard to jurisdictional claims made in the text, published maps, institutional affiliations, or any other geographical representation in this paper. While Copernicus Publications makes every effort to include appropriate place names, the final responsibility lies with the authors. Views expressed in the text are those of the authors and do not necessarily reflect the views of the publisher.

Acknowledgements

We are grateful to Copernicus Climate Data Store for providing ERA5 reanalysis data. We also thank the High Performance Computing Center of Nanjing University of Information Science and Technology for providing the computing resources.

Financial support

This work is jointly supported by grants from the National Natural Science Foundation of China (grant nos. 42361144843, 42322503, and 42230608), the National Research Foundation of Korea (NRF) grant funded by the Korea government (MSIT) (grant no. 2023R1A2C3005607), and the Korea Meteorological Administration Research and Development Program "Enhancement of Convergence Technology of Analysis and Forecast on Severe Weather" (grant no. KMA2018-00121).

https://doi.org/10.5194/essd-2025-836
Preprint. Discussion started: 18 March 2026

References

Bengtsson, L., Hodges, K. I., and Roeckner, E.: Storm Tracks and Climate Change, J. Clim., 19, 3518–3543, https://doi.org/10.1175/JCLI3815.1, 2006.

Brands, S., Gutiérrez, J. M., and San-Martín, D.: Twentieth-century atmospheric river activity along the west coasts of Europe and North America: algorithm formulation, reanalysis uncertainty and links to atmospheric circulation patterns, Clim. Dyn., 48, 2771–2795, https://doi.org/10.1007/s00382-016-3095-6, 2017.

Chen, H.-B. and Rao, J.: A database of objectively identified atmospheric rivers based on a multi-method fusion algorithm, Zenodo [data set], https://doi.org/10.5281/zenodo.18051602, 2025.

Chen, X., Leung, L. R., Gao, Y., Liu, Y., Wigmosta, M., and Richmond, M.: Predictability of Extreme Precipitation in Western U.S. Watersheds Based on Atmospheric River Occurrence, Intensity, and Duration, Geophys. Res. Lett., 45, 11693-11701, https://doi.org/10.1029/2018GL079831, 2018.

Cheng, T. F., Lu, M., Wang, B., and Dai, L.: A Fresh View of the Asian-Australian Monsoon Complexity: The Intertropical Convective Cell (ITCC) Framework, J. Geophys. Res. Atmos., 129, e2023JD039498, https://doi.org/10.1029/2023JD039498, 2024.

Corringham, T. W., McCarthy, J., Shulgina, T., Gershunov, A., Cayan, D. R., and Ralph, F. M.: Climate change contributions to future atmospheric river flood damages in the western United States, Sci. Rep., 12, 13747, https://doi.org/10.1038/s41598-022-15474-2, 2022.

Dettinger, M. D.: Atmospheric Rivers as Drought Busters on the U.S. West Coast, J. Hydrometeorol., 14, 1721–1732, https://doi.org/10.1175/JHM-D-13-02.1, 2013.

Ding, Y., Liang, P., Liu, Y., and Zhang, Y.: Multiscale Variability of Meiyu and Its Prediction: A New Review, J. Geophys. Res. Atmos., 125, e2019JD031496, https://doi.org/10.1029/2019JD031496, 2020.

Eiras-Barca, J., Ramos, A. M., Pinto, J. G., Trigo, R. M., Liberato, M. L. R., and Miguez-Macho, G.: The concurrence of atmospheric rivers and explosive cyclogenesis in the North Atlantic and North Pacific basins, Earth Syst. Dyn., 9, 91–102, https://doi.org/10.5194/esd-9-91-2018, 2018.

Francis, D., Mattingly, K. S., Temimi, M., Massom, R., and Heil, P.: On the crucial role of atmospheric rivers in the two major Weddell Polynya events in 1973 and 2017 in Antarctica, Sci. Adv., 6, eabc2695, https://doi.org/10.1126/sciadv.abc2695, 2020.

Gimeno, L., Algarra, I., Eiras-Barca, J., Ramos, A. M., and Nieto, R.: Atmospheric river, a term encompassing different meteorological patterns, WIREs Water, 8, e1558, https://doi.org/10.1002/wat2.1558, 2021.

Guan, B.: Global Atmospheric Rivers Database, Version 4, UCLA Dataverse [data set], https://doi.org/10.25346/S6/ZSW7UN, 2024.

Guan, B. and Waliser, D. E.: Detection of atmospheric rivers: Evaluation and application of an algorithm for global studies, J. Geophys. Res. Atmos., 120, 12514–12535, https://doi.org/10.1002/2015JD024257, 2015.

https://doi.org/10.5194/essd-2025-836
Preprint. Discussion started: 18 March 2026

Guan, B. and Waliser, D. E.: Tracking Atmospheric Rivers Globally: Spatial Distributions and Temporal Evolution of Life Cycle Characteristics, J. Geophys. Res. Atmos., 124, 12523–12552, https://doi.org/10.1029/2019JD031205, 2019.

Guan, B. and Waliser, D. E.: A regionally refined quarter-degree global atmospheric rivers database based on ERA5, Sci. Data, 11, 440, https://doi.org/10.1038/s41597-024-03258-4, 2024.

Guan, B., Molotch, N. P., Waliser, D. E., Fetzer, E. J., and Neiman, P. J.: Extreme snowfall events linked to atmospheric rivers and surface air temperature via satellite measurements, Geophys. Res. Lett., 37, https://doi.org/10.1029/2010GL044696, 2010.

Guan, B., Waliser, D. E., and Ralph, F. M.: An Intercomparison between Reanalysis and Dropsonde Observations of the Total Water Vapor Transport in Individual Atmospheric Rivers, J. Hydrometeorol., 19, 321–337, https://doi.org/10.1175/JHM-D-17-0114.1, 2018.

Guo, Y., Shinoda, T., Guan, B., Waliser, D. E., and Chang, E. K. M.: Statistical Relationship between Atmospheric Rivers and Extratropical Cyclones and Anticyclones, J. Clim., 33, 7817–7834, https://doi.org/10.1175/JCLI-D-19-0126.1, 2020.

Kamae, Y., Mei, W., Xie, S.-P., Naoi, M., and Ueda, H.: Atmospheric Rivers over the Northwestern Pacific: Climatology and Interannual Variability, J. Clim., 30, 5605–5619, https://doi.org/10.1175/JCLI-D-16-0875.1, 2017.

Kemter, M., Fischer, M., Luna, L. V., Schönfeldt, E., Vogel, J., Banerjee, A., Korup, O., and Thonicke, K.: Cascading Hazards in the Aftermath of Australia's 2019/2020 Black Summer Wildfires, Earths Future, 9, e2020EF001884, https://doi.org/10.1029/2020EF001884, 2021.

Knippertz, P. and Wernli, H.: A Lagrangian Climatology of Tropical Moisture Exports to the Northern Hemispheric Extratropics, J. Clim., 23, 987–1003, https://doi.org/10.1175/2009JCLI3333.1, 2010.

Kwon, Y. and Son, S.-W.: East Asian atmospheric rivers are most hazardous in summer, Weather Clim. Extrem., 44, 100658, https://doi.org/10.1016/j.wace.2024.100658, 2024.

Kwon, Y., Park, C., Son, S.-W., and Kim, J.: Modulation of East Asian atmospheric rivers by the Pacific-Japan teleconnection pattern, Environ. Res. Lett., 19, 064055, https://doi.org/10.1088/1748-9326/ad4fa6, 2024.

Lavers, D. A. and Villarini, G.: The contribution of atmospheric rivers to precipitation in Europe and the United States, J. Hydrol., 522, 382–390, https://doi.org/10.1016/j.jhydrol.2014.12.010, 2015.

Lavers, D. A., Allan, R. P., Wood, E. F., Villarini, G., Brayshaw, D. J., and Wade, A. J.: Winter floods in Britain are connected to atmospheric rivers, Geophys. Res. Lett., 38, https://doi.org/10.1029/2011GL049783, 2011.

Lavers, D. A., Villarini, G., Allan, R. P., Wood, E. F., and Wade, A. J.: The detection of atmospheric rivers in atmospheric reanalyses and their links to British winter floods and the large-scale climatic circulation, J. Geophys. Res. Atmos., 117, https://doi.org/10.1029/2012JD018027, 2012.

Liang, J. and Yong, Y.: Climatology of atmospheric rivers in the Asian monsoon region, Int. J. Climatol., 41, E801–E818, https://doi.org/10.1002/joc.6729, 2021.

Liang, J., Yong, Y., and Hawcroft, M. K.: Long-term trends in atmospheric rivers over East Asia, Clim. Dyn., 60, 643–666, https://doi.org/10.1007/s00382-022-06339-5, 2023.

https://doi.org/10.5194/essd-2025-836
Preprint. Discussion started: 18 March 2026

Lim, E.-P., Hendon, H. H., Boschat, G., Hudson, D., Thompson, D. W. J., Dowdy, A. J., and Arblaster, J. M.: Australian hot and dry extremes induced by weakenings of the stratospheric polar vortex, Nat. Geosci., 12, 896–901, https://doi.org/10.1038/s41561-019-0456-x, 2019.

Mahoney, K., Jackson, D. L., Neiman, P., Abel, M. R., Darby, L., Wick, G., White, A., Sukovich, E., and Cifelli, R.: Understanding the Role of Atmospheric Rivers in Heavy Precipitation in the Southeast United States, Mon. Weather Rev., 144, 1617–1632, https://doi.org/10.1175/MWR-D-15-0279.1, 2016.

Nayak, M. A., Villarini, G., and Lavers, D. A.: On the skill of numerical weather prediction models to forecast atmospheric rivers over the central United States, Geophys. Res. Lett., 41, 4354–4362, https://doi.org/10.1002/2014GL060299, 2014.

Neiman, P. J., Ralph, F. M., White, A. B., Kingsmill, D. E., and Persson, P. O. G.: The Statistical Relationship between Upslope Flow and Rainfall in California's Coastal Mountains: Observations during CALJET, Mon. Weather Rev., 130, 1468–1492, https://doi.org/10.1175/1520-0493(2002)130%253C1468:TSRBUF%253E2.0.CO;2, 2002.

Neiman, P. J., Ralph, F. M., Wick, G. A., Lundquist, J. D., and Dettinger, M. D.: Meteorological Characteristics and Overland Precipitation Impacts of Atmospheric Rivers Affecting the West Coast of North America Based on Eight Years of SSM/I Satellite Observations, J. Hydrometeorol., 9, 22–47, https://doi.org/10.1175/2007JHM855.1, 2008.

Neiman, P. J., Schick, L. J., Ralph, F. M., Abel, M. R., and Wick, G. A.: Flooding in Western Washington: The Connection to Atmospheric Rivers*, J. Hydrometeorol., 12, 1337–1358, https://doi.org/10.1175/2011JHM1358.1, 2011.

Paltan, H., Waliser, D., Lim, W. H., Guan, B., Yamazaki, D., Pant, R., and Dadson, S.: Global Floods and Water Availability Driven by Atmospheric Rivers, Geophys. Res. Lett., 44, 10387-10395, https://doi.org/10.1002/2017GL074882, 2017.

Pan, M. and Lu, M.: A Novel Atmospheric River Identification Algorithm, Water Resour. Res., 55, 6069–6087, https://doi.org/10.1029/2018WR024407, 2019.

Pan, M. and Lu, M.: East Asia Atmospheric River catalog: Annual Cycle, Transition Mechanism, and Precipitation, Geophys. Res. Lett., 47, e2020GL089477, https://doi.org/10.1029/2020GL089477, 2020.

Park, C. and Son, S.-W.: Atmospheric Rivers in East Asia Summer as the Continuum of Extratropical and Monsoonal Moisture Plumes, J. Clim., 37, 5055–5071, https://doi.org/10.1175/JCLI-D-23-0731.1, 2024.

Park, C., Son, S.-W., and Kim, H.: Distinct Features of Atmospheric Rivers in the Early Versus Late East Asian Summer Monsoon and Their Impacts on Monsoon Rainfall, J. Geophys. Res. Atmos., 126, e2020JD033537, https://doi.org/10.1029/2020JD033537, 2021.

Park, C., Son, S.-W., and Guan, B.: Multiscale Nature of Atmospheric Rivers, Geophys. Res. Lett., 50, e2023GL102784, https://doi.org/10.1029/2023GL102784, 2023.

Payne, A. E., Demory, M.-E., Leung, L. R., Ramos, A. M., Shields, C. A., Rutz, J. J., Siler, N., Villarini, G., Hall, A., and Ralph, F. M.: Responses and impacts of atmospheric rivers to climate change, Nat. Rev. Earth Environ., 1, 143–157, https://doi.org/10.1038/s43017-020-0030-5, 2020.

Priestley, M. D. K. and Catto, J. L.: Future changes in the extratropical storm tracks and cyclone intensity, wind speed, and structure, Weather Clim. Dyn., 3, 337–360, https://doi.org/10.5194/wcd-3-337-2022, 2022.

https://doi.org/10.5194/essd-2025-836
Preprint. Discussion started: 18 March 2026

Ralph, F. M. and Dettinger, M. D.: Storms, floods, and the science of atmospheric rivers, Eos Trans. Am. Geophys. Union, 92, 265–266, https://doi.org/10.1029/2011EO320001, 2011.

Ralph, F. M., Neiman, P. J., and Wick, G. A.: Satellite and CALJET Aircraft Observations of Atmospheric Rivers over the Eastern North Pacific Ocean during the Winter of 1997/98, Mon. Weather Rev., 132, 1721–1745, https://doi.org/10.1175/1520-0493(2004)132%253C1721:SACAOO%253E2.0.CO;2, 2004.

Ralph, F. M., Neiman, P. J., Wick, G. A., Gutman, S. I., Dettinger, M. D., Cayan, D. R., and White, A. B.: Flooding on California's Russian River: Role of atmospheric rivers, Geophys. Res. Lett., 33, https://doi.org/10.1029/2006GL026689, 2006.

Ralph, F. M., Coleman, T., Neiman, P. J., Zamora, R. J., and Dettinger, M. D.: Observed Impacts of Duration and Seasonality of Atmospheric-River Landfalls on Soil Moisture and Runoff in Coastal Northern California, J. Hydrometeorol., 14, 443–459, https://doi.org/10.1175/JHM-D-12-076.1, 2013.

Ralph, F. M., Dettinger, M., Lavers, D., Gorodetskaya, I. V., Martin, A., Viale, M., White, A. B., Oakley, N., Rutz, J., Spackman, J. R., Wernli, H., and Cordeira, J.: Atmospheric Rivers Emerge as a Global Science and Applications Focus, Bull. Am. Meteorol. Soc., 98, 1969–1973, https://doi.org/10.1175/BAMS-D-16-0262.1, 2017a.

Ralph, F. M., Iacobellis, S. F., Neiman, P. J., Cordeira, J. M., Spackman, J. R., Waliser, D. E., Wick, G. A., White, A. B., and Fairall, C.: Dropsonde Observations of Total Integrated Water Vapor Transport within North Pacific Atmospheric Rivers, J. Hydrometeorol., 18, 2577–2596, https://doi.org/10.1175/JHM-D-17-0036.1, 2017b.

Ralph, F. M., Dettinger, M. D., Cairns, M. M., Galarneau, T. J., and Eylander, J.: Defining "Atmospheric River": How the Glossary of Meteorology Helped Resolve a Debate, Bull. Am. Meteorol. Soc., 99, 837–839, https://doi.org/10.1175/BAMS-D-17-0157.1, 2018.

Rao, J., Garfinkel, C. I., White, I. P., and Schwartz, C.: The Southern Hemisphere Minor Sudden Stratospheric Warming in September 2019 and its Predictions in S2S Models, J. Geophys. Res. Atmos., 125, e2020JD032723, https://doi.org/10.1029/2020JD032723, 2020.

Risbey, J. S., Pook, M. J., McIntosh, P. C., Wheeler, M. C., and Hendon, H. H.: On the Remote Drivers of Rainfall Variability in Australia, Mon. Weather Rev., 137, 3233–3253, https://doi.org/10.1175/2009MWR2861.1, 2009.

Rutz, J. J., Steenburgh, W. J., and Ralph, F. M.: Climatological Characteristics of Atmospheric Rivers and Their Inland Penetration over the Western United States, Mon. Weather Rev., 142, 905–921, https://doi.org/10.1175/MWR-D-13-00168.1, 2014.

Rutz, J. J., Shields, C. A., Lora, J. M., Payne, A. E., Guan, B., Ullrich, P., O'Brien, T., Leung, L. R., Ralph, F. M., Wehner, M., Brands, S., Collow, A., Goldenson, N., Gorodetskaya, I., Griffith, H., Kashinath, K., Kawzenuk, B., Krishnan, H., Kurlin, V., Lavers, D., Magnusdottir, G., Mahoney, K., McClenny, E., Muszynski, G., Nguyen, P. D., Prabhat, Mr., Qian, Y., Ramos, A. M., Sarangi, C., Sellars, S., Shulgina, T., Tome, R., Waliser, D., Walton, D., Wick, G., Wilson, A. M., and Viale, M.: The Atmospheric River Tracking Method Intercomparison Project (ARTMIP): Quantifying Uncertainties in

https://doi.org/10.5194/essd-2025-836
Preprint. Discussion started: 18 March 2026

Atmospheric River Climatology, J. Geophys. Res. Atmos., 124, 13777–13802, https://doi.org/10.1029/2019JD030936, 2019.

Sayama, T., Yamada, M., Sugawara, Y., and Yamazaki, D.: Ensemble flash flood predictions using a high-resolution nationwide distributed rainfall-runoff model: case study of the heavy rain event of July 2018 and Typhoon Hagibis in 2019, Prog. Earth Planet. Sci., 7, 75, https://doi.org/10.1186/s40645-020-00391-7, 2020.

Shields, C. A., Rutz, J. J., Leung, L.-Y., Ralph, F. M., Wehner, M., Kawzenuk, B., Lora, J. M., McClenny, E., Osborne, T., Payne, A. E., Ullrich, P., Gershunov, A., Goldenson, N., Guan, B., Qian, Y., Ramos, A. M., Sarangi, C., Sellars, S., Gorodetskaya, I., Kashinath, K., Kurlin, V., Mahoney, K., Muszynski, G., Pierce, R., Subramanian, A. C., Tome, R., Waliser, D., Walton, D., Wick, G., Wilson, A., Lavers, D., Prabhat, Collow, A., Krishnan, H., Magnusdottir, G., and Nguyen, P.: Atmospheric River Tracking Method Intercomparison Project (ARTMIP): project goals and experimental design, Geosci. Model Dev., 11, 2455–2474, https://doi.org/10.5194/gmd-11-2455-2018, 2018.

Tsuguti, H., Seino, N., Kawase, H., Imada, Y., Nakaegawa, T., and Takayabu, I.: Meteorological overview and mesoscale characteristics of the Heavy Rain Event of July 2018 in Japan, Landslides, 16, 363–371, https://doi.org/10.1007/s10346-018-1098-6, 2019.

Wang, H.-R.: Atmospheric River (AR) Fused Identification Dataset from 1980 to 2016, Zenodo [data set], https://doi.org/10.5281/zenodo.10229029, 2023.

Wang, H.-R., Li, F.-F., Grigorev, G. V., Yao, Z.-Y., Ge, D., Wang, G.-Q., and Qiu, J.: Occurrence Frequency of Global Atmospheric River (AR) Events: A Data Fusion Analysis of 12 Identification Data Sets, J. Geophys. Res. Atmos., 129, e2023JD039730, https://doi.org/10.1029/2023JD039730, 2024.

Wang, T., Wei, K., and Ma, J.: Atmospheric Rivers and Mei-yu Rainfall in China: A Case Study of Summer 2020, Adv. Atmos. Sci., 38, 2137–2152, https://doi.org/10.1007/s00376-021-1096-9, 2021.

Wick, G. A., Neiman, P. J., and Ralph, F. M.: Description and Validation of an Automated Objective Technique for Identification and Characterization of the Integrated Water Vapor Signature of Atmospheric Rivers, IEEE Trans. Geosci. Remote Sens., 51, 2166–2176, https://doi.org/10.1109/TGRS.2012.2211024, 2013.

Yang, Y., Zhao, T., Ni, G., and Sun, T.: Atmospheric rivers over the Bay of Bengal lead to northern Indian extreme rainfall, Int. J. Climatol., 38, 1010–1021, https://doi.org/10.1002/joc.5229, 2018.

Ye, C., Zhang, H., Moise, A., and Mo, R.: Atmospheric rivers in the Australia-Asian region: a BoM–CMA collaborative study, J. South. Hemisph. Earth Syst. Sci., 70, 3–16, https://doi.org/10.1071/ES19025, 2020.

Zhang, Z., Ralph, F. M., and Zheng, M.: The Relationship Between Extratropical Cyclone Strength and Atmospheric River Intensity and Position, Geophys. Res. Lett., 46, 1814–1823, https://doi.org/10.1029/2018GL079071, 2019.

Zhou, Y., Kim, H., and Guan, B.: Life Cycle of Atmospheric Rivers: Identification and Climatological Characteristics, J. Geophys. Res. Atmos., 123, 12,715-12,725, https://doi.org/10.1029/2018JD029180, 2018.

Zhu, Y. and Newell, R. E.: Atmospheric rivers and bombs, Geophys. Res. Lett., 21, 1999–2002, https://doi.org/10.1029/94GL01710, 1994.

https://doi.org/10.5194/essd-2025-836
Preprint. Discussion started: 18 March 2026

630 Zhu, Y. and Newell, R. E.: A Proposed Algorithm for Moisture Fluxes from Atmospheric Rivers, Mon. Weather Rev., 126, 725–735, https://doi.org/10.1175/1520-0493(1998)126<0725:APAFMF>2.0.CO;2, 1998.